

Strong Interactions in the Problem of Three Black Holes

M. Imbrogno, C. Meringolo, and S. Servidio*

Dipartimento di Fisica, Università della Calabria, I-87036 Cosenza, Italy

(Dated: May 3, 2022)

We study the three-body problem from different perspectives, going from Newtonian physics to general relativity. In the classical case, we model the interactions in a typical chaotic configuration, identifying Strong Interaction Times (SITs), namely transients in which the system manifests complex, highly-energetic dynamics. By selecting these SITs as initial data for the general relativistic case, we perform a campaign of simulations of numerical relativity. To provide a comprehensive menu of cases, we investigate different global configurations. By comparing with the more “quiet” two-body inspiral, we observe strong nonlinear emission of gravitational waves. The multi-body signals have been inspected by employing both Fourier and wavelet analyses, showing net differences among the global configurations. The wavelet analysis reveals the reminiscence of the SITs in the three black holes problem. Such a survey of simulations might be a guide for future observations.

I. INTRODUCTION

The three-body problem represents the non-linear problem *par excellence* [1]. There are several applications of this problem, going from microphysics to large-scale astrophysics. In this cross-scale variety of examples, the problem remains puzzling, despite years of studies, since the bodies have an erratic behavior (see [2] for a review). From the classical perspective, for example, in problems of celestial mechanics, one may almost always identify a binary and a third body. A binary can be treated as a single entity with certain internal properties (like a molecule). The couple interacts with a third body, once or more frequently, with a resultant change in the internal properties of the binary. During the interaction, the system conserves the total energy, the mass, the momentum, and the angular momentum, even though the trajectories of the single bodies are unpredictable [1, 3]. During the complex dynamics, the system redistributes energy and angular momentum efficiently; as three-body scattering goes on, the population may gain speed and become ‘heated’. This has profound consequences on the structure and evolution of clusters. Three (or many)-body interactions are therefore expected to be common in clusters and galactic cores [4]. Multiple black holes might also be formed in galactic nuclei undergoing sequential mergers [2, 5], triple quasar systems [6], in globular clusters and galactic disks [7–9].

There is a good chance of having, at some point of the interaction, the three bodies strongly dominated by their mutual gravitational attraction. In this regime, when masses are large, the chaotic three-body dynamics should be treated via general relativistic models, and, when distances are on the order of the gravitational radii, merging events are likely to occur [10, 11]. In globular clusters, indeed, N -body interactions are important in the formation of massive black holes [12–14]. In such a system, the conservation of the classic invariants needs to be revised in terms of general relativity [15, 16].

The mergers of compact massive objects represent the most suggestive and extraordinary events in nature. According to general relativity, these systems are powerful sources of gravitational waves – disturbances of the spacetime. However, the gravitational radiation, detected through modern experimental settings, cannot unambiguously characterize what happens in the vicinity of the merging region, and complementary studies of numerical relativity are needed [17–21]. It is, therefore, crucial to construct guidance for future observational campaigns, by exploring a wide class of possibilities for the three-body configurations, by varying for example parameters such as their initial distribution, their initial global angular momentum, their spin, and their masses. The understanding of such strong, nonlinear interactions represents a new challenge for the comprehension of cosmological problems and needs to be tackled via appropriate models, following the Einstein’s vision of gravitation [22, 23].

In this work, we investigate the main features of the three-body problem, going from classical mechanics to general relativity (GR). We start with the study of the behavior of three point-like bodies according to the classical Newton’s laws. By using a Lagrangian numerical model, we initially consider a geometrical distribution, known as the *the Burrau problem* [16]. Subsequently, we study the same problem by varying the global momentum and the masses, to build a carpet for the study of the analogous dynamics in the case of highly-massive objects. In the second part, we perform direct numerical simulations of GR, by using as initial data the conditions coming from the Newtonian case. We finally inspect the waveform of the gravitational radiation emitted from the system, comparing it with a two-body inspiral. These studies might be useful for the description and the understanding of gravitational signals [24–26].

The paper is organized as follows. In Section II, we summarize the classical results of the chaotic motion of the three-body problem, by solving numerically the equation of motion and by introducing measurements of strong body interactions. In Section III, we tackle the problem from the point of view of general relativity, by

* sergio.servidio@fis.unical.it

introducing a 3+1 formalism to integrate the Einstein field equations, presenting the Spectral-Filtered Numerical Gravity code (SFINGE). Simulations of multi-black hole dynamics are presented in Section IV, comparing the outcome of two black hole (2-BHs for brevity) inspiraling with the three-black hole dynamics initiated via the Newtonian code. Here we highlight the main differences via different spectral analyses of the produced signal, away from the sources. Finally, conclusions are discussed in Section V.

II. THREE-BODIES IN THE NEWTONIAN CASE

Despite the success in the understanding of simple (reduced) cases [1, 27], the solution to the general three-body problem remained elusive for about 200 years after the publication of Newton's *Principia*. In the general three-body problem, all three masses are all on the same order and their initial positions and velocities are not arranged in any particular way. The difficulty of such a problem derives from the fact that there are no coordinate transformations that simplify the problem. This is in contrast to the two-body case where the solutions are found most easily in the center-of-mass coordinate system. In the three-body case, such transformation does not alleviate the problem, a difficulty which made the system analytically rather intractable, up to the modern age of computers. The numerical approach, indeed, revealed that the orbits are good examples of chaos in nature [28–30]. As follows, we run through again the main numerical results of the classical problem.

The system of equations describing the multi-body system of N point-like masses M_i , affected only by their mutual gravitational forces, is given by:

$$\dot{\mathbf{x}}_i = \mathbf{v}_i, \quad (1)$$

$$M_i \dot{\mathbf{v}}_i = - \sum_{j \neq i}^N \frac{M_i M_j}{|\mathbf{r}_i - \mathbf{r}_j|^2} \hat{\mathbf{r}} = - \sum_{j \neq i}^N M_i M_j \frac{\mathbf{r}_i - \mathbf{r}_j}{|\mathbf{r}_i - \mathbf{r}_j|^3}, \quad (2)$$

where we have used the geometrical units $c = G = 1$, \mathbf{r}_i is the position of the i^{th} body, \mathbf{v}_i is its velocity, and $N = 3$ represents the number of bodies. We numerically solved the above equations, by using a fourth-order Runge-Kutta technique, with quadruple precision. We start with a particular initial configuration of the three-body problem that immediately leads to a chaotic motion, namely the so-called *Pythagorean problem* proposed by Burrau in the early '90s [31]. The point-like bodies, whose masses are $M_1 = 3$, $M_2 = 4$ and $M_3 = 5$, are initially at the corners of a Pythagorean triangle. These are located essentially on a xy -plane ($z = 0$), as reported in Fig. 1 (a) with (colored) bullets of mass-proportional size.

In the beginning, the bodies are all at rest. Burrau's calculation revealed the typical behavior of a three-body system: two bodies approach each other have a close

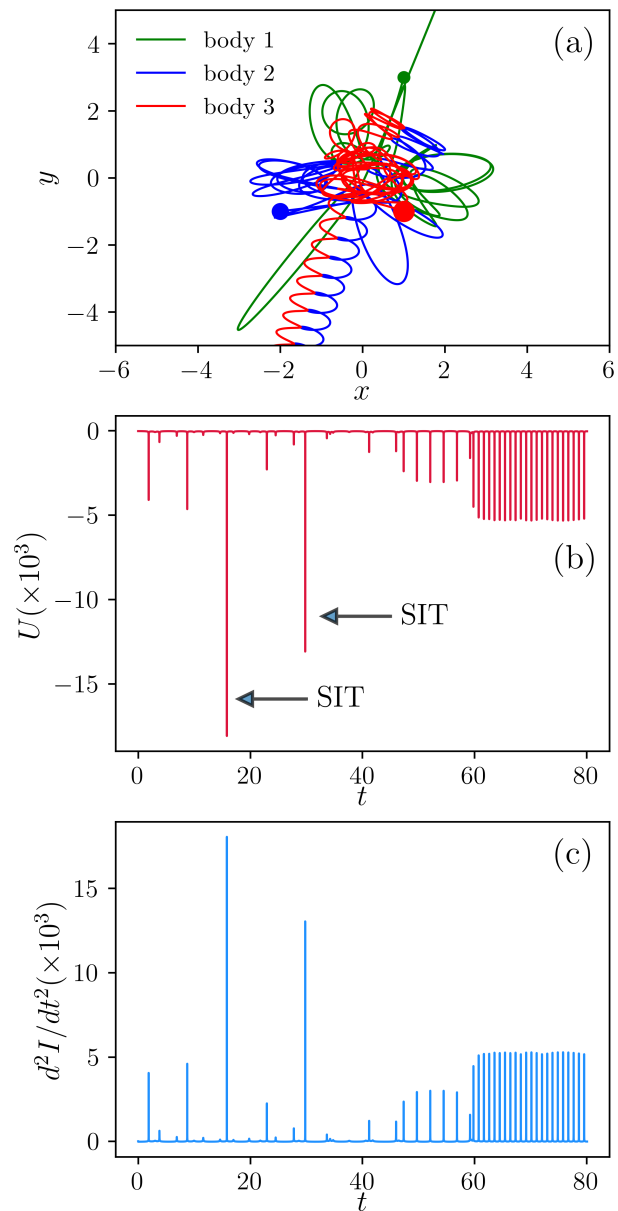


FIG. 1. Overview of the Burrau three-body problem in the classical case. (a) Trajectories starting from the Burrau configuration (the initial position of the bodies are emphasized by the colored balls), up to $t = 80$. (b) Time history of the potential energy. (c) Second time-derivative of the momentum of inertia for the system. Spikes in (b) and (c) correspond to typical SITs.

encounter, and then recede again. Subsequently, other two-body encounters were calculated by Burrau until he came to the end of his calculating capacity. Later work has shown that the solution to the problem is quite typical of initially bound three-body systems. After many close two-body approaches a configuration arises which leads to an escape of one body and the formation of a binary by the other two bodies [1], as represented in Fig. 1 (a), where we report the trajectories of the three bodies up to $t = 80$ for the chosen configuration.

We measured the kinetic T , the potential U , and the

TABLE I. Initial parameters of the classical simulations in the four cases investigated. The values are reported in geometrical units, so the initial positions and velocities are normalized to the total mass of the system M .

Run Name	a Classical Burrau	b Equal masses	c Normalized masses	d Spinning Burrau
M_1	3.0	0.33	0.25	0.25
M_2	4.0	0.33	0.33	0.33
M_3	5.0	0.33	0.42	0.42
\mathbf{r}_1/M	(1, 3, 0)	(1, 3, 0)	(1, 3, 0)	(1, 3, 0)
\mathbf{r}_2/M	(-2, -1, 0)	(-2, -1, 0)	(-2, -1, 0)	(-2, -1, 0)
\mathbf{r}_3/M	(1, -1, 0)	(1, -1, 0)	(1, -1, 0)	(1, -1, 0)
\mathbf{v}_1/M	(0, 0, 0)	(0, 0, 0)	(0, 0, 0)	(-0.299, 0.050, 0)
\mathbf{v}_2/M	(0, 0, 0)	(0, 0, 0)	(0, 0, 0)	(0.149, -0.100, 0)
\mathbf{v}_3/M	(0, 0, 0)	(0, 0, 0)	(0, 0, 0)	(0.059, 0.050, 0)

total energy E of the system, as a function of time, until a single body and the binary leave apart, which happens at about $t \approx 60$. The potential energy, representative of the gravitational interaction, is reported in Fig. 1 (b). These interactions are extraordinarily intermittent. We call these bursts Strong Interaction Times (SITs), where two (or all) of the three bodies are particularly close and the system has very large potential (and kinetic) energy. At later times, one can note that, for $t \gtrsim 60$, we have small, periodic energy spikes. This is because, at about this time, the system is split into a (regular) binary system and a single-motion body, so we lose the stochastic behavior typical of three bodies systems. This phenomenon of the “escaper” is largely investigated in the literature [1]. To characterize the system configuration in the most energetic periods, we measured the moment of inertia $I = \sum M_i r_i^2$ and its acceleration $\dot{I} = d^2 I / dt^2$. As reported in Fig. 1 (c), \dot{I} peaks exactly at the SITs, as expected. Note that differentiating the moment of inertia twice with respect to time one obtains the Lagrange-Jacobi identity $\dot{I} = 4T + 2U$. The latter can be viewed as a unique identifier of a SIT event. The importance of \dot{I} lies in the fact that it is a measure of the compactness of the three-body system and hence it might be important if one wants to consider GR effects.

To explore the parameter space, we performed a simulation campaign varying with respect the Burrau case (Run a) the masses and the overall angular momentum (and hence velocities of the single bodies). The cases are summarized in Table I. In the case with equal masses, Run b, we essentially have the same Burrau configuration as in Run a, but with total mass being unity. Similarly, in Run c, we have the same conditions of Run a, but re-scaling the masses such that again the total mass in the system is one. Finally, in the “Spinning Burrau case” (Run d), we choose non-zero initial velocities, such that the total angular momentum remains conserved. Here the whole system has a global spin, which somehow confines the masses to interact in a limited region of space. This case might be of interest for modeling global galaxies coalescence.

In Fig. 2 we present an overview of all the Newtonian

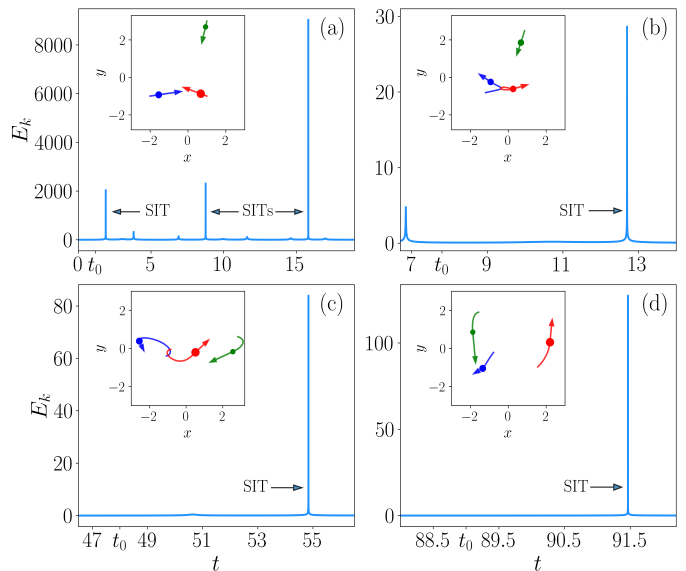


FIG. 2. Overview of the kinetic energy time history for each of the classic cases, namely, Run a–d in Table I (each label corresponds to a configuration). In the insets, we show the position of the bodies, with mass-proportional bullets size, and the direction of the velocity vectors at the pre-SIT time t_0 . This time has been highlighted with an arrow.

simulations summarized in Table I. In each panel, we represent the total kinetic energy of the system, concentrating therefore on time windows near strong nonlinear interactions instants. In the inset of each panel, we report the position of the three bodies at a time that precedes a SIT. We labeled such time as t_0 and it will be of practical interest for our GR experiments (see later). Moreover, we also report mass-proportional bullets, with the respective velocity arrows of the bodies, to give a global overview of each SIT event. The systems are all long-living and chaotic.

These numerical simulations might be of interest for celestial bodies with small masses, but they are unrealistic when it comes to massive bodies. In particular, it is natural to ask what happens when three large compact objects collide during a SIT. To answer such a question,

one has to tackle the problem from a completely different perspective, invoking GR. We use the Newtonian configurations at the quiet times before SITs, namely at t_0 , as initial data for numerical relativity, exploring therefore the spacetime dynamics of Run a–d. In the next section, we provide the theoretical and numerical background for the GR investigation.

III. NUMERICAL RELATIVITY

The loss of energy and angular momentum from the system via gravitational radiation changes the basic constants of the three-body problem, and general relativity effects need to be incorporated. Such radiation leads to a decay of a binary orbit, and finally to a collapse of the binary black hole system into a single black hole. The final decay stages are very rapid and this might dramatically change the evolution of the three-body problem in the case of singular spacetimes. What happens to three black holes when they strongly interact? The final result might be the escape of one of the black holes and the recoil of the binary in the opposite direction, or it can be the subsequent merging of the three massive objects [16, 22, 23]. We will focus on the interaction of the three black holes to extract the gravitational waves generated due to the loss of energy and angular momentum from the system, by varying also the initial configuration, as described in Table I. To understand such emission, we will compare the two-body inspiraling with the three-body case.

We now introduce numerical techniques adequate for the stable and accurate evolution of multiple black-hole spacetimes. In particular, the techniques will be based on the *moving puncture* approach [32], treated by a novel pseudo-spectral method [33]. The whole system will be evolved based on the Baumgarte-Shapiro-Shibata-Nakamura formulation of Einstein’s equations [34–36] (hereafter BSSN, for brevity), with a highly structured and accurate code. The formulation starts from a conformal re-scaling of the physical metric

$$\gamma_{ij} = \psi^4 \tilde{\gamma}_{ij}, \quad (3)$$

where ψ is a conformal factor. We follow the approach of Campanelli [32], where this factor is written as $\chi = \psi^{-4}$. This choice has been demonstrated to be a better alternative when considering singular spacetimes for which ψ typically has a r^{-1} singularity, while χ is a C^4 function at the singularity. By following this procedure, the Ricci tensor can be separated into two contribution, $R_{ij} = \tilde{R}_{ij} + R_{ij}^X$, where

$$\begin{aligned} \tilde{R}_{ij} = & -\frac{1}{2} \tilde{\gamma}^{lm} \partial_l \partial_m \tilde{\gamma}_{ij} + \tilde{\gamma}_{k(i} \partial_{j)} \tilde{\Gamma}^k + \tilde{\Gamma}^k \tilde{\Gamma}_{(ij)k} \\ & + \tilde{\gamma}^{lm} \left(2\tilde{\Gamma}_{l(i}^k \tilde{\Gamma}_{j)km} + \tilde{\Gamma}_{im}^k \tilde{\Gamma}_{klj} \right) \end{aligned}$$

is the Ricci tensor related to the conformal metric and

$$\begin{aligned} R_{ij}^X = & \frac{1}{2\chi} \left\{ \left[\partial_i \partial_j \chi - \frac{\partial_i \chi \partial_j \chi}{2\chi} - \tilde{\Gamma}_{ij}^k \partial_k \chi \right] \right. \\ & \left. + \tilde{\gamma}_{ij} \left[\tilde{\gamma}^{lm} \left(\partial_l \partial_m \chi - \frac{3 \partial_l \chi \partial_m \chi}{2\chi} \right) - \tilde{\Gamma}^k \partial_k \chi \right] \right\} \end{aligned}$$

is the part that depends on the conformal factor χ . In the BSSN approach, the extrinsic curvature K_{ij} is divided in two independent variables, the trace K and its trace-free parts A_{ij} . The last one is subjected to the same conformal transformation described by equation (3), i.e. $\tilde{A}_{ij} = \chi(K_{ij} - \frac{1}{3}\gamma_{ij}K)$. Finally, a new field is introduced, namely the contracted Christoffel symbols associated with the conformal metric $\tilde{\Gamma}^i = \tilde{\gamma}^{jk} \tilde{\Gamma}_{jk}^i$.

With the above change of variables, the system of BSSN equations reads:

$$\partial_0 \tilde{\gamma}_{ij} = -2\alpha \tilde{A}_{ij}, \quad (4)$$

$$\partial_t \chi = \frac{2}{3} \chi (\alpha K - \partial_i \beta^i) + \beta^i \partial_i \chi, \quad (5)$$

$$\partial_0 K = -D^2 \alpha + \alpha \left(\tilde{A}_{lm} \tilde{A}^{lm} + \frac{1}{3} K^2 \right), \quad (6)$$

$$\partial_0 \tilde{A}_{ij} = \chi \left[-D_i D_j \alpha + \alpha R_{ij} \right]^{TF} + \alpha \left(K \tilde{A}_{ij} - 2\tilde{A}_{ik} \tilde{A}_j^k \right), \quad (7)$$

$$\begin{aligned} \partial_t \tilde{\Gamma}^i = & \tilde{\gamma}^{lm} \partial_l \partial_m \beta^i + \frac{1}{3} \tilde{\gamma}^{il} \partial_l \partial_m \beta^m + \beta^k \partial_k \tilde{\Gamma}^i \\ & - \tilde{\Gamma}^k \partial_k \beta^i + \frac{2}{3} \tilde{\Gamma}^i \partial_k \beta^k - 2\tilde{A}^{ik} \partial_k \alpha \\ & + \alpha \left(2\tilde{\Gamma}_{lm}^i \tilde{A}^{lm} - \frac{3}{\chi} \tilde{A}^{ik} \partial_k \chi - \frac{4}{3} \tilde{\gamma}^{ik} \partial_k K \right). \end{aligned} \quad (8)$$

In the above set note that $\partial_0 = \partial_t - \mathcal{L}_\beta$, where \mathcal{L}_β is the Lie derivative with respect to the shift β^k , α is the lapse, D_i is the covariant derivative associated with the physical three-metric γ_{ij} , and $D^2 = \gamma^{ij} D_i D_j$. Notice that Eq.s (5) and (8) are reported with ∂_t derivatives rather than ∂_0 derivatives. As usual, “TF” indicates the trace-free part of a tensor. To close the system, we need the evolution equation for the lapse and the shift, choosing therefore the slicing conditions. In the framework of the Bona-Massó formalism [35, 37, 38], we choose

$$\partial_0 \alpha = -\alpha^2 f(\alpha) K, \quad (9)$$

$$\partial_0 \beta^i = \frac{3}{4} B^i, \quad (10)$$

$$\partial_0 B^i = \partial_t \tilde{\Gamma}^i - \beta^j \partial_j \tilde{\Gamma}^i - \eta B^i. \quad (11)$$

Here η is a positive constant and is set to $\eta = 2.8$ [39], the factor $3/4$ is somewhat arbitrary but leads to good numerical results, and $f(\alpha)$ is an arbitrary function which is set to $f(\alpha) = 1/\alpha$ and corresponds to the “1 + log” slicing conditions common in black holes simulations.

In addition to the evolution equations, as discussed in [41–45], the BSSN variables must satisfy the vacuum

TABLE II. Parameters of the BSSN simulations, based on the Newtonian cases in Table I, at a given time t_0 before SITs. The values are reported in geometrical units. The last line indicates the initial ADM mass, evaluated as suggested in [40].

RUN Name	I 2 BHs	II Classical Burrau	III Equal masses	IV Normalized masses	V Spinning Burrau	VI Intrinsic Spin
M_1	0.45	3.0	0.33	0.25	0.25	0.25
M_2	0.45	4.0	0.33	0.33	0.33	0.33
M_3	//	5.0	0.33	0.42	0.42	0.42
\mathbf{r}_1/M	(0, 1.151, 0)	(0.931, 2.695, 0)	(0.671, 1.857, 0)	(2.554, -0.172, 0)	(-1.874, 0.856, 0)	(-1.874, 0.856, 0)
\mathbf{r}_2/M	(0, -1.151, 0.0)	(-1.544, -0.931, 0)	(-0.929, -0.242, 0)	(-2.557, 0.385, 0)	(-1.352, -1.048, 0)	(-1.352, -1.048, 0)
\mathbf{r}_3/M	//	(0.676, -0.872, 0)	(0.259, -0.615, 0)	(0.513, -0.205, 0)	(2.206, 0.325, 0)	(2.206, 0.325, 0)
\mathbf{v}_1/M	(0.335, 0, 0)	(-0.037, -0.039, 0)	(-0.119, -0.358, 0)	(-0.296, -0.132, 0)	(0.036, -0.382, 0)	(0.036, -0.382, 0)
\mathbf{v}_2/M	(-0.335, 0, 0)	(0.251, 0.037, 0)	(-0.336, 0.229, 0)	(0.034, -0.070, 0)	(-0.059, -0.035, 0)	(-0.059, -0.035, 0)
\mathbf{v}_3/M	//	(-0.179, 0.066, 0)	(0.455, 0.129, 0)	(0.150, 0.135, 0)	(0.025, 0.258, 0)	(0.025, 0.258, 0)
\mathbf{J}_1/M^2	(0, 0, 0)	(0, 0, 0)	(0, 0, 0)	(0, 0, 0)	(0, 0, 0)	(0, 0, 0.100)
\mathbf{J}_2/M^2	(0, 0, 0)	(0, 0, 0)	(0, 0, 0)	(0, 0, 0)	(0, 0, 0)	(0, 0, -0.050)
\mathbf{J}_3/M^2	(0, 0, 0)	(0, 0, 0)	(0, 0, 0)	(0, 0, 0)	(0, 0, 0)	(0, 0, -0.050)
M_{ADM}	0.904	12.001	1.003	1.004	1.008	1.007

constraints

$$\mathcal{H} = R - \tilde{A}_{lm} \tilde{A}^{lm} + \frac{2}{3} K^2 = 0, \quad (12)$$

$$\mathcal{M}^i = \partial_k \tilde{A}^{ik} + \tilde{\Gamma}_{lm}^i \tilde{A}^{lm} - \frac{3}{2\chi} \tilde{A}^{ik} \partial_k \chi - \frac{2}{3} \tilde{\gamma}^{ik} \partial_k K = 0, \quad (13)$$

$$\mathcal{G}^i = \tilde{\Gamma}^i + \partial_j \tilde{\gamma}^{ij} = 0, \quad (14)$$

$$\tilde{\gamma} - 1 = 0, \quad (15)$$

$$\tilde{A} = 0, \quad (16)$$

where $\tilde{\gamma}$ is the determinant of the conformal metric, and \tilde{A} is the trace of \tilde{A}_{ij} . During the numerical simulations, we enforce the algebraic constraints in equations (15), and (16). The remaining constraints, \mathcal{H} , \mathcal{M}^i and \mathcal{G}^i are not actively enforced and are used to monitor the accuracy of the numerical solutions [39]. In all the above equations, $\tilde{\Gamma}^i$ is replaced by $-\partial_j \tilde{\gamma}^{ij}$, wherever it is not differentiated.

A. The SFINGE code

The numerical procedure is described in Meringolo et al. [33] and has been tested against all classical testbeds. The spatial derivatives are computed in Cartesian geometry, via standard FFTs. For each BSSN field $f(x^\mu) \equiv f(\mathbf{x}, t)$, the equations have been discretized on an equally-spaced lattice of $N_x \times N_y \times N_z$ mesh points. At the collocation points, $f(\mathbf{x}, t) = \sum_{\mathbf{k}} \tilde{f}_{\mathbf{k}}(t) \exp(i\mathbf{k} \cdot \mathbf{x})$, with \mathbf{x} being the positions of the nodes, $\tilde{f}_{\mathbf{k}}(t) \in \mathbb{Z}$ the Fourier coefficients and the wavevectors $\mathbf{k} = (k^x, k^y, k^z)$. Along each box side L_0 , the wavevector is $k = 2\pi m/L_0$, with $m = 0, \pm 1, \pm 2, \dots, \pm N_k$, where $N_k = N/2$ is the Nyquist mode. The code is based on parallel architecture and makes use of MPI directives and FFTW libraries.

In the spectral space, the nonlinear terms become a convolution and there are several transform-based techniques for evaluating it efficiently [46–48]. Numerical problems might arise because of the so-called *aliasing instabilities* [49]: any product among fields creates higher k 's, causing an alias when these new modes become larger than the maximum size N_k of sampled Fourier modes. A Fourier mode with a wavenumber out of the size range is aliased to another wavenumber in the domain and, in a time-evolving system, it creates growing numerical problems. The importance of eliminating such pathology (aliasing) has been studied since pioneering works by Orszag et al. [50]. We use a strategy to mitigate such problems based on an analogy with compressible hydrodynamics, by using a filtering technique [51–53]. In practice, for each representation one has

$$f(\mathbf{x}, t) = \sum_{\mathbf{k}} \tilde{f}_{\mathbf{k}}(t) e^{ik_j x^j} \Phi_{k^*}(\mathbf{k}), \quad (17)$$

where the spectral anti-aliasing filter is given by $\Phi_{k^*}(\mathbf{k}) = e^{-a \left[\frac{|\mathbf{k}|}{k^*} \right]^2}$. Here a is a free parameter (we set $a = 20$) that gives the sharpness of the filter and k^* is again the cutoff. Different values of k^* have been chosen, depending on the difficulty of the simulation and on the initial data. Hereafter we set $k^* = N/2.5$, where $N = 512$ is the number of grid points along each spatial direction.

For the time integration, we adopt a second-order Runge-Kutta method, with a time-step that can be changed during the evolution, as described in [33]. Finally, we introduce an implicit, viscous strategy to absorb boundary disturbances, typical of the numerical tests that have a small violation of the periodicity. Loosely speaking, we use Cartesian geometries in order to simulate spherical domains and dissipate the regions close to the corners, with a radial envelope [54–56]. Hyperviscous terms of the type $\nu_n \nabla^n f$ (where ν_n is a numerical coefficient) can dissipate quickly ripples and numerical artifacts. For any dynamical BSSN variable, we advance in time the solution $f^{\{ideal\}}(\mathbf{x}, t)$ by using the

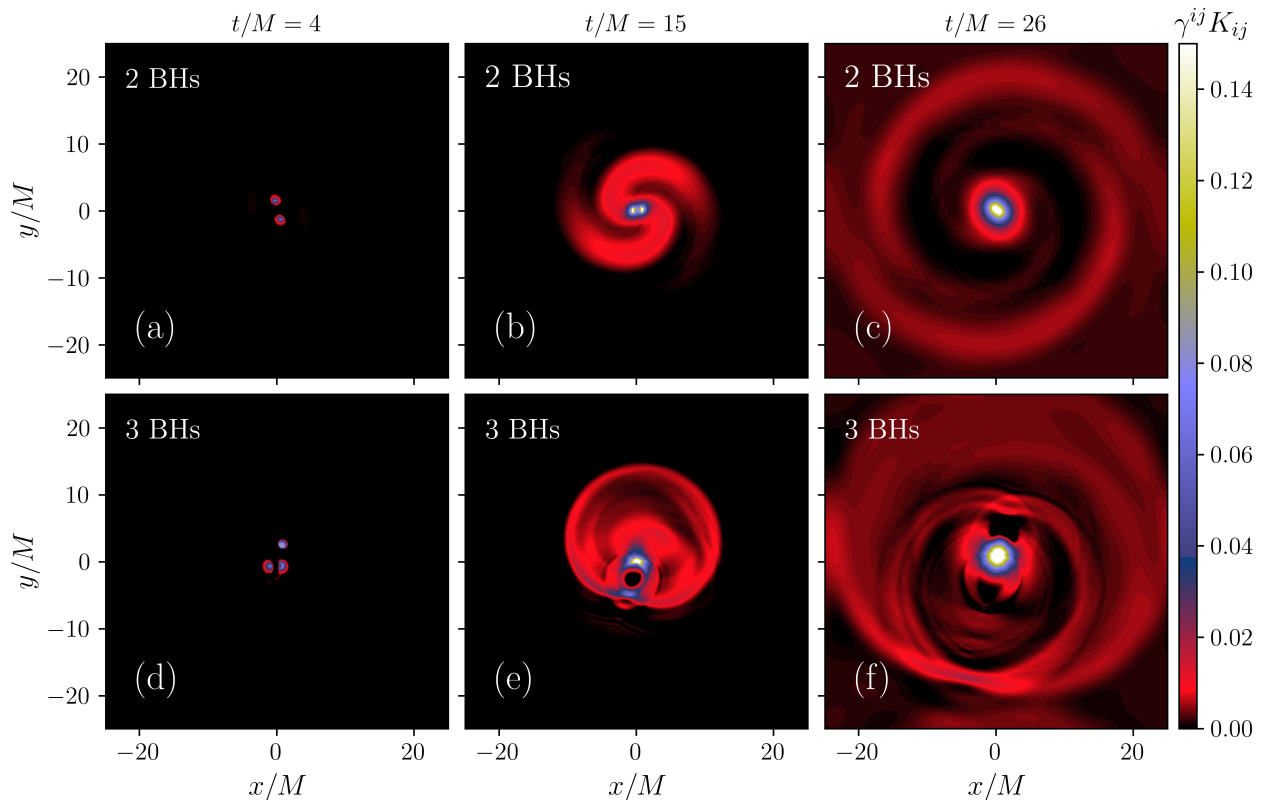


FIG. 3. Shaded contours of the extrinsic curvature K for the two black holes (RUN I, top row) and the three-body ‘Classical Burrau’ interaction (RUN II, bottom row), at three different times of the evolution, that is before, during, and after merger.

classical second-order Runge-Kutta method. Simultaneously, we evolve in time an accompanying, twin-field $f^{\{H\}}(\mathbf{x}, t)$ which obeys the same BSSN equation but is also subject to hyperviscous dissipation, being therefore highly damped. We advance in time this hyperviscous field $f^{\{H\}}(\mathbf{x}, t)$ by using a Crank-Nicolson, semi-implicit method. With this procedure, the internal ideal region, advanced via the Runge-Kutta method, is matched with the outer diffusive layer integrated via the implicit scheme. Overall, the price to pay is that we have to double the time of integration, slowing down the computation. On the other hand, the method gives clear benefits on the stability and the goodness of the solutions [53].

IV. MULTIPLE BLACK HOLES DYNAMICS

The SFINGE code also includes modules to build initial data for a variety of problems, in a self-consistent way. The starting point for multiple black hole data without boost and spin is the Schwarzschild solution in isotropic coordinates. In the case of time symmetry, these conformally flat data can be generalized to an arbitrary number of black holes by adding the individual contribution in the conformal factor $\psi = \chi^{-1/4}$. This initial configuration of multiple black holes is known as Brill-Lindquist data [57]. For boosted black holes, the conformal factor is written

as $\psi = 1 + \sum_i \frac{M_i}{2r_i} + u$, where M_i and r_i are respectively the mass parameter and the distance from the i^{th} black hole, and u is a corrective term [58]. To build the initial condition for multiple black holes with arbitrary boost and spin, one has to solve an elliptic equation for u . We have used an iterative Gauss-Seidel algorithm [59], starting from an initial guess, as specified in Cao et al. [60].

The initial data for multiple black holes require more conditions and a longer convergence time for the iterative algorithm. In particular, these calculations might take several CPU hours by using the above Gauss-Seidel technique. To accelerate the convergence, we start on a low-resolution initial cube (64^3 mesh points), solving the Hamiltonian constraint relatively quickly. Then, to interpolate on a greater lattice, we first move in the Fourier space by increasing the number of k -vectors via zero-padding, and then we obtain the physical fields performing an inverse FFT. This allows us to have a better initial guess on the higher-resolution box, with a much faster converge rate. By iterating this technique, adapting recursively (by interpolation) the solution to finer grids, we finally get the initial data.

Concerning the simulation parameters, for all the BSSN simulations, the domain is represented by a cube of side $L_0 = 50M$, with 512^3 mesh points. The time step is initially chosen to be $\Delta t = 8 \times 10^{-3}$. Furthermore, we control, for each case, that the Hamiltonian and the

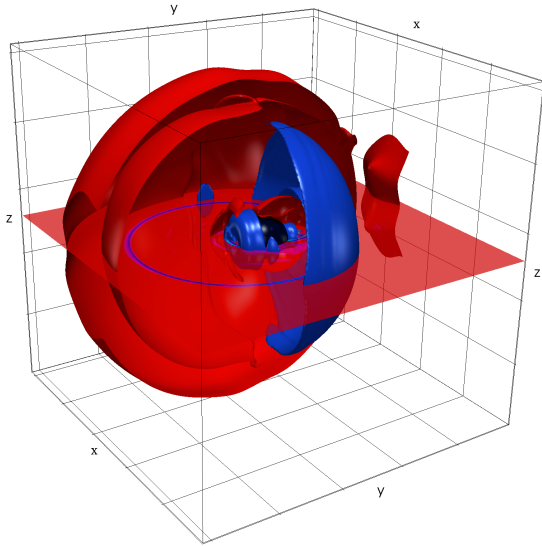


FIG. 4. 3D representation of the three-black hole interaction, at time $t/M = 26$ for RUN II (“Classical Burräu” in Table II). The (red and blue) isosurfaces represent constant values of the extrinsic curvature K , outside from the final black hole (central black-shaded region). The 2D plane represents a color contour of the Newman-Penrose scalar Ψ_4 .

momentum constraints are well satisfied. The parameters of the BSSN simulations are summarized in Table II and are labeled with roman numbers. In particular, we are interested in the fully-relativistic evolution of the classical system when it is approaching a SIT, controlling that, at t_0 , the BHs are sufficiently apart.

Before treating the complex three-body problem, we first calibrate our numerical experiments via the two-body inspiraling, which will provide us with the classical waveform [61–63]. The scope is to compare the properties of the gravitational waves generated from both the binary and the three-body systems. The numerical experiment describes the evolution of two compact objects of equal masses that are initially placed symmetrically with respect to the center of the box. They have a small initial velocity which is the same for both bodies but in opposite directions, and the properties of such “2 BHs” configuration are summarized in Table II as RUN I. As expected, the BHs spiral around each other covering a single orbital period before merging, as shown in Fig. 3. A simple, fast way to identify a gravitational disturbance is to look at a scalar measure of the value of the extrinsic curvature, especially in the ecliptic plane. As can be seen from panels (a)–(c), small amplitude waves propagate out during the merger. After that, a large amplitude modulation propagates away, once the two event horizons come into contact [64–68]. At this point, several disturbances of smaller amplitude begin to propagate until the system converges into a Kerr-type black hole.

In the second campaign of GR simulations, we describe

the evolution of 3-BHs, inspired by Run a–d. In particular, we take from these cases the initial data at t_0 , as described in Fig. 2. With this strategy, by using spectral methods, we can concentrate on events that might be energetically relevant (and hence detectable by experiments.) As reported in Table II, RUN II represents the “Classical Burräu”, as in Run *a*; RUN III (“Equal masses”) describes a similar system, but this time the masses of the black holes are equal, as in Run *b*; as in Run *c*, the “Normalized masses” (RUN IV) describes the same problem for three black holes having different masses normalized such that $M = 1$. All the above configurations refer to the case in which the three bodies are at rest at the very beginning, so we do not expect any global inspiraling. The “Spinning Burräu” (Run V) covers this case, namely the initial configuration is such that the angular momentum is different from zero (Run *d*). We performed the last simulation, proper of GR, named “Intrinsic spin” (RUN VI), which presents the same initial setup as RUN V, except that the BHs have their own spin.

Focusing on the overview of K reported in Fig. 3 (d)–(f), one can see how, compared to the 2-BHs, the patterns are more distorted, with finer scales. The configuration lacks a global spiraling motion, due to the absence of global angular momentum. In the post-merging phase, after the system has been allowed to “relax”, it is possible to see a different pattern for the extrinsic curvature, suggesting a different kind of asymptotic solution for the final black hole. In Fig. 4, we report a full-dimensional rendering of this RUN II, where we represent the gravitational radiation after the subsequent merging events. The (red and blue) shaded contours represent the isosurfaces of constant K , at two different values, showing how the outgoing waves are irregular and skewed. The region close to the final event horizon is represented with a (black) sphere.

To get more insight into the multi-black hole dynamics, we analyze the waveform by computing the projection of the Newman-Penrose scalar Ψ_4 , which quantifies the radiation from a source of gravitational waves. This standard procedure represents the relativistic analog of the Poynting theorem in electromagnetism [34, 69–73]. After we computed this scalar by following the procedure described in [74, 75], we interpolated Ψ_4 from a Cartesian to a spherical grid, on which we calculated the outgoing radiation via the spin-weighted spherical harmonic $Y_{22}^{(-2)}(\theta, \varphi)$. This projection extracts the dominant contribution of the emitted waves, which comes from the quadrupole mode ($l = 2, m = 2$). In Fig. 4, we report the (color) contour of Ψ_4 in the equatorial xy -plane (at $z/M = 25$), for the three-body case (RUN II). The outgoing gravitational radiation is evident.

We compare all the signals coming from these multiple-black hole cases, by looking at the outgoing radiation as measured away from the sources. We evaluated the above projection at a given distance from the center of the box, namely at $r^* = 20M$, as a function of time, while the disturbances fly through the virtual detector. The signals

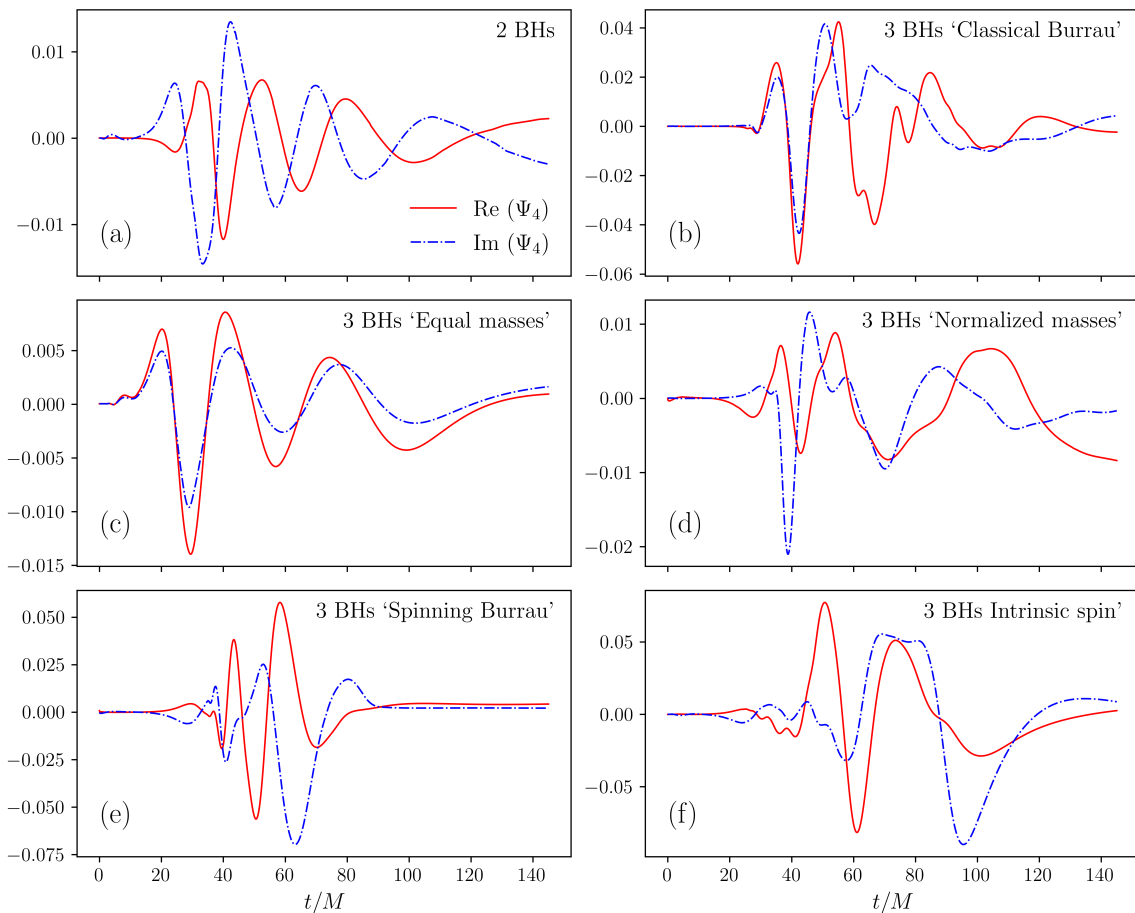


FIG. 5. Reconstruction of the gravitational wave signal for (a) the binary black hole system and (b)–(f) the three-black holes systems, namely RUNs I–VI in Table II. The solid (dotted) lines represent the real (imaginary) part of the spherical projection of Ψ_4 . All the simulations are performed up to $t/M = 145$. The three-black hole cases reveal a more structured and nonlinear behavior.

are depicted in Fig. 5, revealing net differences among the cases. First, contrary to the case of the binary [panel (a)], the real and imaginary parts of the waveform of some of the 3-BHs cases are almost in phase. Second, while for the 2-BHs only one peak can be observed (corresponding to the single merger), in the other cases multiple-scale disturbances are present, due to the subsequent collapses. Third, the signal from the three-body problem is much more irregular and unpredictable, revealing the presence of higher-order nonlinearities [16, 22, 23, 32, 41, 65, 76]. These more structured signals demand a deeper statistical investigation, performed as follows.

To further highlight the differences among the configurations, identifying possible peculiarities of the 3-BHs interaction, we performed a spectral analysis of the metric disturbances in Fig. 5. As a first step, we smoothed the boundaries via a *generalized normal window*, then we computed the Fourier transform and hence the power spectrum. We cross-checked the spectrum with an analogous procedure, by using the Blackman-Tukey technique [77], transforming the windowed auto-correlation function of the signal. The spectrum has been computed for both the real and the imaginary parts of the projection

in Fig. 5. Finally, to decrease statistical uncertainties, we produced an average of the powers. As can be noticed from these averaged power spectra in Fig. 6, the 3-BHs cases produce in general a broader distribution of frequencies. The excess of high frequencies reflects the small scales features observed in the vicinity of the three-body system, already noticed in Figs. 3 and 4. The narrower spectrum is observed for the binary system and for RUN III, in which the head-on of the smallest black holes did not produce enough nonlinearity. On the other hand, the “Spinning Burrau” case produces the smallest scales of our campaign of simulations. It is worth noticing that in the three-body case the spectrum manifests a power-law behavior for $0.6 < \omega < 3$, stimulating interesting speculations about the possibility of a *gravitational turbulent cascade*. However, the classical one-dimensional Fourier spectrum alone cannot say too much about the nature of the dynamics, since the processes are highly non-stationary. In this regard, we shall proceed with a refined analysis, described hereafter.

Because of the non-stationarity of the signal, we analyze the wavefront by employing a wavelet decomposition. The main feature of wavelets is their natural split-

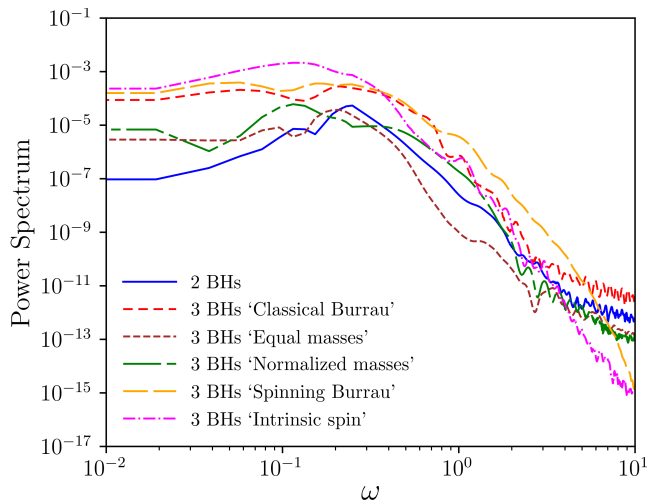


FIG. 6. Power spectrum of the waveforms in Fig. 5. The spectrum represent an average over the power spectra of the two signals (real and imaginary part of the projection of the Newman-Penrose scalar Ψ_4).

ting of fluctuations into different scale components according to the multiscale resolution analysis [78], being therefore a powerful tool of investigation for multi-body coalescence events. Among the several choices, all of them qualitatively consistent with each other, the clearest results are here obtained for the Shannon generating function [79]. This reconstruction makes use of the “sinc function”, which is very localized and rapidly decaying to zero – very adequate for the presence of discrete frequencies although less performant for time-localization [80, 81]. Such a typical wavelet spectrogram is reported in Fig. 7, where we take into consideration three characteristic cases: RUN I, II, and V. The 2-BHs case manifests a clear single peak in frequency, corresponding to the merging event. A rise-up in frequency can be seen for $5 < t < 40$, typical of the inspiral phase [32, 65]. Real and imaginary signals of the scalar have very similar behavior. At a later time, the system shows the typical low-frequency modulation of the resultant, perturbed black hole. Very different is the behavior of the 3-BHs. In the Classical Burrau, by looking at $Re\{\Psi_4\}$, apart from the main frequency similar to the 2-BHs due to the first head-on merger, there are secondary peaks. There is a secondary peak at $t \sim 75$ and $f \sim 0.08$, due to the follow-up disturbance that propagates from the secondary SIT, when the larger BH *eats* the remaining one. This corresponds to a disturbance coming from large mass ratio coalescence. Finally, we performed the same analysis for the case with the broadest Fourier spectrum in Fig. 6, namely for RUN V. In the Spinning Burrau, indeed, the BHs are confined by the large global angular momentum. This constraint forces the 2 mergings to happen at about the same time, with multiple nonlinear effects. This highly nonlinear interaction can be observed as a net broadening of the wavelet spectrum. In this case,

the outgoing gravitational waves are carrying away from the final event horizon the reminiscence of such extreme interaction.

V. CONCLUSIONS

The three-body problem is a classical example of complex dynamics, where the three interacting masses experience a chaotic behavior. We concentrated on two different approaches, namely (1) the Newtonian approach and (2) Einstein’s theory of general relativity. Regarding the first part, we summarized the classical results and developed a very accurate Lagrangian code that solves the trajectories of the bodies, starting from the Pythagorean configuration. Such configuration immediately tends toward a nonlinear regime. During the evolution, the system experiences quiet transients, as well as very bursty behaviors, typical of chaos intermittency [82]. We solved the trajectories accurately and identified such most intense spikes, the SITs. In the second (and more challenging) part, we built a gravitational model to study the dynamics of SITs in terms of GR. By using a sequence of conformal transformations, we briefly introduced the BSSN equations. With equations in hand, we summarized the main properties of the SFINGE code, an algorithm based on a filtered pseudo-spectral scheme.

As guidance for our GR experiments, we considered the problem of the binary, in the final stage of their coalescence, inside the innermost stable circular orbit (ISCO). To measure the emitted gravitational waves, we dealt with the problem of wave extraction. By using a spherical interpolation, and following the Newman-Penrose formalism, we measured the outgoing gravitational waves, as classically done for compact objects simulations. After the two-body simulations, we finally considered the three black hole interaction. We extracted from the Newtonian simulations the initial data preceding a strong SIT, when the bodies are sufficiently apart. We monitored several quantities, such as the metric tensor and the extrinsic curvature of the system, that suggest intense emission during the multiple-coalescence events. In analogy with the 2-BHs, we used the numerical extraction technique and reconstructed the emitted waveform, which is highly irregular and nonlinear. We compared finally the binary merger and the strong three-body interaction, by computing the power spectra of the signals for all the cases. We found net differences, essentially at high frequencies, where the 3-BHs system exhibits a broader distribution of power. The spectrum seems consistent with a power-law distribution which might suggest that gravitation, similarly to hydrodynamics, is subject to a turbulent cascade. To get more insight into the outcome of the multi-BH radiation, we performed a refined analysis of the signals. In particular, we made use of a Shannon wavelet. This analysis reveals net differences between the 2- and the 3-BHs cases. While in the former the projection evidences a single dominating frequency, in the 3-BHs the wavelets

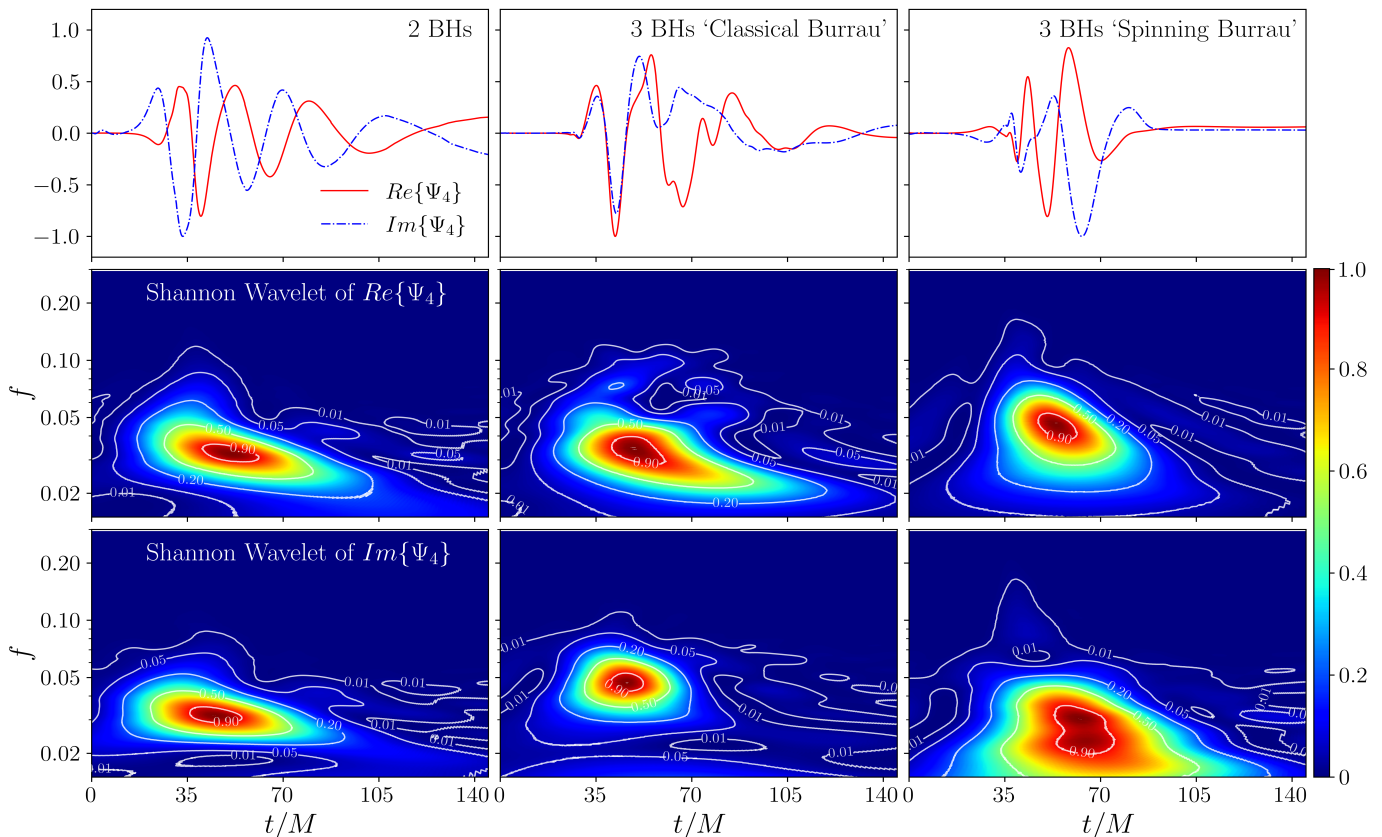


FIG. 7. Spectrogram of the Shannon wavelet (second and third row) for three different waveforms (first row), namely for RUN I (left), RUN II (center), and RUN V (right). In the middle and bottom row, we report the wavelet analysis for the real and the imaginary part of Ψ_4 , respectively. The signals and the spectra have been normalized here to one to favor the comparison.

suggest that there are multiple frequencies produced during the evolution, due to the multiple SITs. Finally, in the case in which there is a global angular momentum that confines the BHs, there is a net broadening of the wavelet power, typical of nonlinear phenomena.

While the 2-BHs inspiral has been largely investigated in literature [60, 63, 67, 83–88], there is much less documentation about 3-BHs SITs [15, 16] and, at the present, there is no observational evidence. These results could be of interest for future observational campaigns, since we expect that, with modern technologies, one can achieve better signal-to-noise sensibility, investigating whether

such spectacular events might sometimes occur in the Universe. In future works, we will inspect the statistical properties of the gravitational fields in such nonlinear regimes, by performing larger, higher-resolution, and longer numerical experiments.

ACKNOWLEDGMENTS

The simulations have been performed at the Newton HPPC Computing Facility, at the University of Calabria.

-
- [1] V. M. J. Valtonen, and H. Karttunen, *The three-body problem* (Cambridge University Press, 2006).
- [2] M. J. Valtonen, *Monthly Notices of the Royal Astronomical Society* **278**, 186 (1996).
- [3] J. Monaghan, *Monthly Notices of the Royal Astronomical Society* **177**, 583 (1976).
- [4] M. C. Miller and D. P. Hamilton, *The Astrophysical Journal* **576**, 894 (2002).
- [5] J. Makino and P. Hut, *The Astrophysical Journal* **365**, 208 (1990).
- [6] S. G. Djorgovski, F. Courbin, G. Meylan, D. Sluse, D. Thompson, A. Mahabal, and E. Glikman, *The Astrophysical Journal Letters* **662**, L1 (2007).
- [7] K. Gültekin, M. C. Miller, and D. P. Hamilton, in *AIP Conference Proceedings* (American Institute of Physics, 2003), vol. 686, pp. 135–140.
- [8] S. J. Berukoff and B. M. Hansen, *The Astrophysical Journal* **650**, 901 (2006).
- [9] A. Gualandris, S. Portegies Zwart, and M. S. Sipior, *Monthly Notices of the Royal Astronomical Society* **363**, 223 (2005).
- [10] F. Antonini, N. Murray, and S. Mikkola, *The Astrophysical*

- ical Journal **781**, 45 (2014).
- [11] J. Samsing, M. MacLeod, and E. Ramirez-Ruiz, *The Astrophysical Journal* **784**, 71 (2014).
- [12] K. Gültekin, M. Miller, and D. Hamilton (2003).
- [13] M. C. Miller and N. Yunes, *Nature* **568**, 469 (2019).
- [14] K. Gültekin, M. C. Miller, and D. P. Hamilton, *The Astrophysical Journal* **616**, 221 (2004).
- [15] P. Galaviz, B. Brügmann, and Z. Cao, *Physical Review D* **82**, 024005 (2010).
- [16] C. O. Lousto and Y. Zlochower, *Physical Review D* **77**, 024034 (2008).
- [17] F. Pretorius, *Physical review letters* **95**, 121101 (2005).
- [18] F. Pretorius, *Classical and Quantum Gravity* **23**, S529 (2006).
- [19] D. Ceverino, A. Dekel, D. Tweed, and J. Primack, *Monthly Notices of the Royal Astronomical Society* **447**, 3291 (2015).
- [20] F. Bounaud, P.-A. Duc, and E. Emsellem, *Monthly Notices of the Royal Astronomical Society: Letters* **389**, L8 (2008).
- [21] L. Lehner and F. Pretorius, *Annual Review of Astronomy and Astrophysics* **52**, 661 (2014).
- [22] M. Campanelli, C. O. Lousto, and Y. Zlochower, *Physical Review D* **77**, 101501(R) (2008).
- [23] K. Silsbee and S. Tremaine, *The Astrophysical Journal* **836**, 39 (2017).
- [24] K. Danzmann, L. S. Team, et al., *Classical and Quantum Gravity* **13**, A247 (1996).
- [25] M. Armano, M. Benedetti, J. Bogenstahl, D. Bortoluzzi, P. Bosetti, N. Brandt, A. Cavalleri, G. Ciani, I. Cristofolini, A. Cruise, et al., *Classical and Quantum Gravity* **26**, 094001 (2009).
- [26] J. Baker, T. Baker, C. Carbone, G. Congedo, C. Contaldi, I. Dvorkin, J. Gair, Z. Haiman, D. F. Mota, A. Renzini, et al., *Experimental Astronomy* pp. 1–30 (2021).
- [27] H. Goldstein, C. Poole, and J. Safko, Reading, MA **426** (1980).
- [28] R. A. Mardling, in *The Cambridge N-Body Lectures* (Springer, 2008), pp. 59–96.
- [29] S. Liao, *Communications in Nonlinear Science and Numerical Simulation* **19**, 601 (2014).
- [30] P. T. Boyd and S. L. McMillan, *Chaos: An Interdisciplinary Journal of Nonlinear Science* **3**, 507 (1993).
- [31] C. Burrau, *Astronomische Nachrichten* **195**, 113 (1913).
- [32] M. Campanelli, C. O. Lousto, P. Marronetti, and Y. Zlochower, *Phys. Rev. Lett.* **96**, 111101 (2006).
- [33] C. Meringolo, S. Servidio, and P. Veltri, *Classical and Quantum Gravity* (2021).
- [34] M. Alcubierre, *Introduction to 3+1 numerical relativity*, vol. 140 (Oxford University Press, 2008).
- [35] T. W. Baumgarte and S. L. Shapiro, *Physical Review D* **59**, 024007 (1998).
- [36] M. Shibata and T. Nakamura, *Physical Review D* **52**, 5428 (1995).
- [37] C. Bona and J. Massó, *Physical Review D* **40**, 1022 (1989).
- [38] C. Bona, J. Masso, E. Seidel, and J. Stela, *Physical Review Letters* **75**, 600 (1995).
- [39] M. Alcubierre, G. Allen, C. Bona, D. Fiske, T. Goodale, F. S. Guzmán, I. Hawke, S. H. Hawley, S. Husa, M. Koppitz, et al., *Classical and Quantum Gravity* **21**, 589 (2003).
- [40] T. W. Baumgarte, *Physical Review D* **62**, 024018 (2000).
- [41] Y. Zlochower, J. G. Baker, M. Campanelli, and C. O. Lousto, *Physical Review D* **72**, 024021 (2005).
- [42] A. Akbarian and M. W. Choptuik, *Physical Review D* **92**, 084037 (2015).
- [43] A. M. Alekseenko, arXiv preprint gr-qc/0405080 (2004).
- [44] C. Gundlach and J. M. Martin-Garcia, *Physical Review D* **74**, 024016 (2006).
- [45] J. D. Brown, *Physical Review D* **79**, 104029 (2009).
- [46] C. Canuto, M. Y. Hussaini, A. Quarteroni, A. Thomas Jr, et al., *Spectral methods in fluid dynamics* (Springer Science & Business Media, 2012).
- [47] M. Boyle, L. Lindblom, H. P. Pfeiffer, M. A. Scheel, and L. E. Kidder, *Physical Review D* **75**, 024006 (2007).
- [48] J. W. Cooley and J. W. Tukey, *Mathematics of computation* **19**, 297 (1965).
- [49] M. Hossain, W. H. Matthaeus, and S. Ghosh, *Computer physics communications* **69**, 1 (1992).
- [50] S. A. Orszag, *Journal of the Atmospheric sciences* **28**, 1074 (1971).
- [51] U. Frisch, S. Kurien, R. Pandit, W. Pauls, S. S. Ray, A. Wirth, and J.-Z. Zhu, *Physical review letters* **101**, 144501 (2008).
- [52] C.-W. Shu, W.-S. Don, D. Gottlieb, O. Schilling, and L. Jameson, *Journal of Scientific Computing* **24**, 1 (2005).
- [53] C. Meringolo and S. Servidio, *General Relativity and Gravitation* **53**, 1 (2021).
- [54] K. Schneider and M. Farge, *Physical review letters* **95**, 244502 (2005).
- [55] W. Dobler, M. Stix, and A. Brandenburg, *The Astrophysical Journal* **638**, 336 (2006).
- [56] S. Servidio, V. Carbone, L. Primavera, P. Veltri, and K. Stasiewicz, *Planetary and Space Science* **55**, 2239 (2007).
- [57] J. M. Bowen and J. W. York Jr, *Physical Review D* **21**, 2047 (1980).
- [58] S. Brandt and B. Brügmann, *Physical Review Letters* **78**, 3606 (1997).
- [59] F. Albu, J. Kadlec, N. Coleman, and A. Fagan, in *IEEE Workshop on Signal Processing Systems* (IEEE, 2002), pp. 109–114.
- [60] Z. Cao, H.-J. Yo, and J.-P. Yu, *Physical Review D* **78**, 124011 (2008).
- [61] J. Baker, B. Brügmann, M. Campanelli, C. O. Lousto, and R. Takahashi, *Physical Review Letters* **87**, 121103 (2001).
- [62] J. Baker, M. Campanelli, C. O. Lousto, and R. Takahashi, *Physical Review D* **65**, 124012 (2002).
- [63] J. G. Baker, J. Centrella, D.-I. Choi, M. Koppitz, and J. van Meter, *Physical Review D* **73**, 104002 (2006).
- [64] R. N. Lang and S. A. Hughes, *Physical Review D* **74**, 122001 (2006).
- [65] J. Centrella, J. G. Baker, B. J. Kelly, and J. R. van Meter, *Reviews of Modern Physics* **82**, 3069 (2010).
- [66] R. Cotesta, A. Buonanno, A. Bohé, A. Taracchini, I. Hinder, and S. Ossokine, *Physical Review D* **98**, 084028 (2018).
- [67] B. Brügmann, W. Tichy, and N. Jansen, *Physical review letters* **92**, 211101 (2004).
- [68] U. Sperhake, E. Berti, and V. Cardoso, *Comptes Rendus Physique* **14**, 306 (2013).
- [69] F. D. Villalba, P. Bargueño, A. F. Vargas, and E. Contreras, *Physics of the Dark Universe* **30**, 100614 (2020).
- [70] E. T. Newman and R. Penrose, *Scholarpedia* **4**, 7445 (2009).

- [71] S. Campbell and J. Wainwright, *General Relativity and Gravitation* **8**, 987 (1977).
- [72] D. A. B. Iozzo, M. Boyle, N. Deppe, J. Moxon, M. A. Scheel, L. E. Kidder, H. P. Pfeiffer, and S. A. Teukolsky, *Physical Review D* **103**, 024039 (2021).
- [73] T. W. Baumgarte and S. L. Shapiro, *Numerical relativity: solving Einstein's equations on the computer* (Cambridge University Press, 2010).
- [74] B. Brügmann, J. A. González, M. Hannam, S. Husa, U. Sperhake, and W. Tichy, *Physical Review D* **77**, 024027 (2008).
- [75] C. Reisswig, C. D. Ott, U. Sperhake, and E. Schnetter, *Physical Review D* **83**, 064008 (2011).
- [76] P. Anninos, K. Camarda, J. Massó, E. Seidel, W.-M. Suen, and J. Towns, *Physical Review D* **52**, 2059 (1995).
- [77] R. B. Blackman and J. W. Tukey, *Bell System Technical Journal* **37**, 185 (1958).
- [78] I. Daubechies, *Ten lectures on wavelets* (SIAM, 1992).
- [79] M. Unser, *Proceedings of the IEEE* **88**, 569 (2000).
- [80] C. Cattani, *Mathematical Problems in Engineering* **2008** (2008).
- [81] S. Mallat, *A wavelet tour of signal processing* (Elsevier, 1999).
- [82] A. Lichtenberg and M. Lieberman, *Regular and Chaotic Dynamics*, 2nd ed.(Springer-Verlag, New York, NY, 1992) **38**, 49 (1992).
- [83] M. Campanelli, C. O. Lousto, and Y. Zlochower, *Physical Review D* **73**, 061501(R) (2006).
- [84] W. Tichy, *Physical Review D* **74**, 084005 (2006).
- [85] U. Sperhake, *Classical and Quantum Gravity* **32**, 124011 (2015).
- [86] B. Vaishnav, I. Hinder, F. Herrmann, and D. Shoemaker, *Physical Review D* **76**, 084020 (2007).
- [87] M. Campanelli, C. O. Lousto, and Y. Zlochower, *Physical Review D* **74**, 041501(R) (2006).
- [88] W. Tichy, *Physical Review D* **80**, 104034 (2009).